Scilight

Sustainable Engineering Novit
https://www.sciltp.com/journals/sen

Article

Check for updates

Efficient and Reversible Bisphenol A Removal Study Based on Hydrophilic Molecularly Imprinted Polymers-Functionalized Semi-IPN Hydrogel

Zhipeng Chen [1,†], Yufan Zhang [1,†], Xiaole Li [1], Jie Zhao [1], Wenzheng Xie [1], Liming Kong [1], Seitkhan Azat [2] and Qin Xu [1,*]

[1] Institute of Innovation Materials and Energy, School of Chemistry and Materials, Yangzhou University, Yangzhou 225002, China
[2] Laboratory of Engineering Profile, Satbayev University, Almaty 050013, Kazakhstan
* Correspondence: xuqin@yzu.edu.cn; Tel.: +86-524-8797-5244
† These authors contributed equally to this work.

How To Cite: Chen, Z.; Zhang, Y.; Li, X.; et al. Efficient and Reversible Bisphenol A Removal Study Based on Hydrophilic Molecularly Imprinted Polymers-Functionalized Semi-IPN Hydrogel. *Sustainable Engineering Novit* **2026**, *2*(2), 3. https://doi.org/10.53941/sen.2026.100008

Received: 3 February 2026
Revised: 12 May 2026
Accepted: 27 May 2026
Published: 12 June 2026

Abstract: Bisphenol A (BPA), as a typical endocrine-disrupting compound, is present in water and severely threatens both ecosystems and human health. This study reports the doping of hydrophilic molecularly imprinted polymers (MIPs) into an N-isopropylacrylamide/carboxymethyl chitosan (N/C) semi-interpenetrating network (semi-IPN) hydrogel to yield a novel gel membrane (MIP@N/C) with exceptional adsorption performance for BPA. Experimental results revealed that MIP@N/C exhibited a maximum BPA adsorption capacity of 113.66 mg/g, with its adsorption behavior well-described by the Freundlich isotherm and pseudo-second-order kinetic models. The ethanol-triggered solvent responsiveness of MIP@N/C facilitated its rapid elution regeneration. The material retained 99% of its initial adsorption efficiency after six cycles, and even after twelve cycles the removal efficiency remained as high as 97.73%, demonstrating outstanding regenerability. This work overcomes the limitations of traditional adsorbents, such as poor selectivity and difficulty in recovery, providing a new strategy for the efficient removal of pollutants from water.

Keywords: molecular imprinting; Bisphenol A; hydrogel membrane; adsorption

1. Introduction

Bisphenol A (BPA), a typical endocrine-disrupting compound (EDC), is widely employed in manufacturing plastics such as polycarbonates and epoxy resins. According to the Chinese "Standards for Drinking Water Quality" (GB 5749-2022), the maximum allowable concentration of BPA in water is 10 μg/L. However, many evidences suggested that long-term, low-dose exposure of BPA can induce toxicological effects even at concentrations substantially below this regulatory threshold [1]. The occurrence of BPA in various aquatic environments is now ubiquitous. For instance, Zhang et al. [2] detected six bisphenol analogues , including BPA, in tap water samples collected from multiple regions across China. Consequently, the development of efficient and selective technologies for removing BPA from water sources is of paramount importance.

Adsorption has emerged as a prevalent method for BPA removal, primarily due to its operational simplicity and rapid kinetics [3]. Molecularly imprinted polymers (MIPs) are attractive because of their predefined recognition sites, high selectivity, low cost and high static capacity [4,5]. However, conventional MIPs are typically hydrophobic and tend to aggregate in water, which limits site accessibility and adsorption efficiency. This limitation can be overcome by incorporating hydrophilic functional monomers (e.g., acrylamide derivatives)

or water-compatible cross-linkers (e.g., polyvinyl alcohol) during MIP synthesis [6]. In addition, their particulate form leads to difficult recovery and slow regeneration.

Membrane-based adsorption technology presents a compelling alternative by integrating adsorption and separation into a single unit, offering superior stability, mechanical strength, operational simplicity, and efficient solid–liquid separation compared to particulate adsorbents [7,8]. Hydrogel-based membranes have attracted significant attention due to their three-dimensional water-rich networks, which provide abundant accessible sites and facilitate rapid mass transfer, enhancing adsorption performance [9,10]. Representative studies, such as the PVA/PEO/SiO_2–Au nanoparticle composite hydrogel [11] and PNIPAm/PEGDA membranes with nanoscale hydrophobic cavities [12], demonstrate that rational incorporation of functional nanostructures can significantly improve membrane adsorption capacity.

A critical limitation of hydrogel membrane is their compromised mechanical strength in the swollen state, which is often characterized by low mechanical strength and poor toughness, thereby limiting their practical application in water treatment [13]. Interpenetrating network (IPN) hydrogels, composed of rigid, densely cross-linked networks interwoven with flexible, loosely cross-linked networks, improve mechanical stability and toughness [14,15]. This interplay between these two independents yet mutually penetrating networks leads to remarkable enhancements in tensile properties and structural stability. Another effective strategy involves the design of nanocomposite hydrogels, where nanoparticles are homogeneously dispersed throughout the hydrogel matrix via ionic, hydrogen, or coordination bonds. Under external stress, the polymer chains extend, distributing the stress uniformly throughout the network and thereby improving the mechanical performance of the hydrogel membrane [16].

Integrating molecular imprinting technology with IPN hydrogel membranes allows the formation of functional membranes for selective separation of target molecules. Currently, the widely used fabrication techniques for molecularly imprinted hydrogels include bulk polymerization and surface polymerization. Bulk polymerization involves mixing all reaction components in solution followed by polymerization, with the imprinted sites distributed within the hydrogel network. However, water-induced swelling changes the hydrogel volume, distorting the imprinted cavity structure and decreasing site specificity [17,18]. Surface polymerization forms imprinted sites on the hydrogel surface. However, since these sites are exposed externally, the surface-imprinted layer is susceptible to detachment from mechanical stress as the gel film swells and deforms upon water uptake [19,20]. Both methods ultimately lead to a reduction in the regeneration performance of the molecularly imprinted hydrogel membrane.

Combining interpenetrating network hydrogels with particle composites can endow hydrogel membranes with enhanced mechanical properties, thereby avoiding performance loss due to membrane damage during aqueous adsorption [21]. However, common composite materials still suffer from limitations such as poor hydrophilicity, inhomogeneous dispersion within the hydrogel matrix, and insufficient adsorption selectivity. For instance, conventional hydrophobic MIPs tend to aggregate in the hydrogel, significantly reducing the accessibility of imprinted sites [22]; while some nanofillers can offer large surface areas but often suffer from poor selectivity towards specific pollutants [23].

To address these issues, a hydrophilic molecularly imprinted polymer (MIP) was synthesized via free radical polymerization using hydrophilic 2-acrylamido-2-methylpropanesulfonic acid (AMPS) as a functional monomer, as illustrated in Figure 1. This MIP was subsequently incorporated as an additive into a semi-interpenetrating network (semi-IPN) hydrogel composed of NIPAM and carboxymethyl chitosan (CMCS). This design offers several advantages. The use of AMPS as a hydrophilic monomer endows the MIPs with excellent water dispersibility, overcoming the aggregation problem of conventional hydrophobic MIPs and ensuring accessibility of the recognition sites. Embedding MIP particles into the semi IPN hydrogel composed of NIPAM and carboxymethyl chitosan not only solves the difficult recovery issue of MIP particles but also utilizes the porous network structure of the hydrogel to facilitate mass transfer. Moreover, the imprinted cavities exist independently within the hydrogel, so that the swelling changes of the hydrogel do not lead to the loss of imprinted sites. The interfacial hydrogen bonding network formed between the MIP and the N/C hydrogel suppresses excessive swelling, protects the imprinted cavities, and synergistically enhances both adsorption capacity and cycle stability. Compared with other recently reported MIP membrane systems [24], our work achieves superior adsorption capacity and outstanding reusability, while the ethanol/water triggered “co nonsolvency” effect provides a mild and efficient regeneration mechanism.

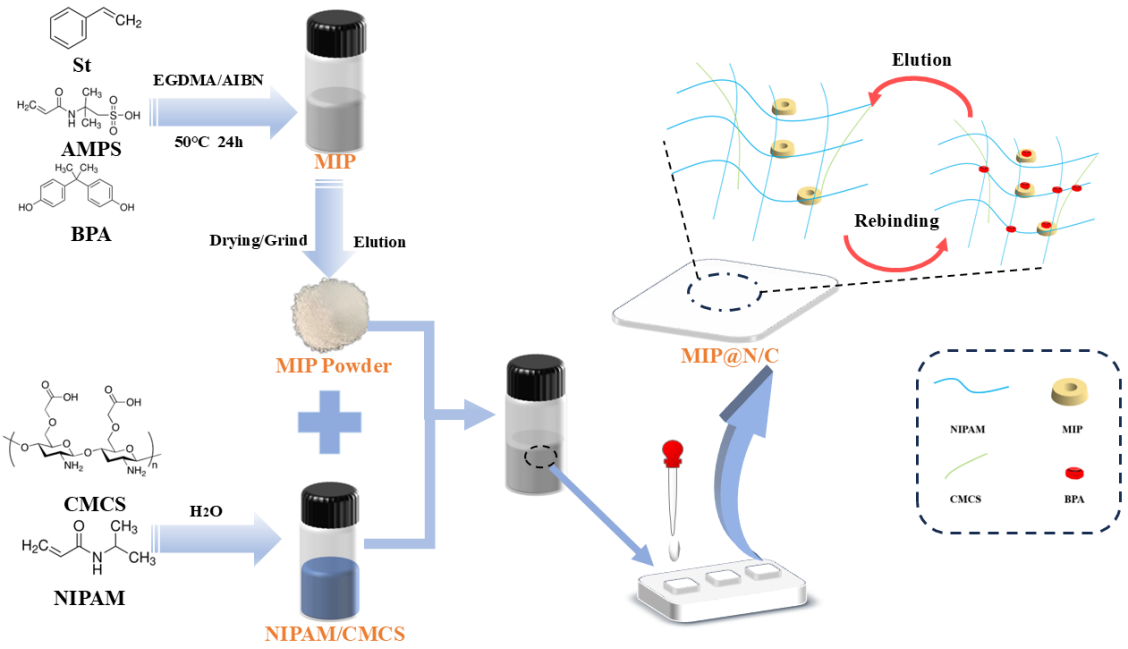

Figure 1. Schematic diagram of the preparation of MIP@N/C.

2. Experimental

2.1. Materials

Bisphenol A (BPA), p-tert-Butylphenol (PTBP) and Bisphenol F (BPF) were bought from Macklin Biochemical Co., Ltd. (Shanghai, China). N-isopropylacrylamide (NIPAM), 2-acrylamido-2-methylpropanesulfonic acid (AMPS), styrene (St), ethylene glycol dimethacrylate (EGDMA) and azobisisobutyronitrile (AIBN) were supplied by Aladdin Biochemical Technology Co., Ltd. (Shanghai, China). Anhydrous ethanol (EtOH), carboxymethyl chitosan (CMCS), N,N-dimethylformamide (DMF), N,N'-methylenebisacrylamide (MBA), tetramethylethylenediamine (TEMED), methanol (MeOH), acetic acid (AcOH) and ammonium persulfate (APS) were purchased from Sinopharm Group Co. Ltd. (Shanghai, China).

The Fourier Transform infrared spectrometer (FT-IR) (Cray 610/670, Varian Inc., Palo Alto, CA, USA) was used to characterize the functional groups of MIP, BPA@MIP, BPA, N/C and MIP0.06@N/C3%. A spectrometer (LAMBDA 650, PerkinElmer Inc., Shanghai, China) was used for Ultraviolet-visible (UV-vis) adsorption analysis. A high-performance liquid chromatography (HPLC) system (Shimadzu LC-20A, Shimadzu Corporation, Kyoto, Japan) was used for the chromatographic analysis with the injection volume 25 μL, and the column temperature 25 °C. A methanol/water mixture (50:50, *v*/*v*) served as the mobile phase at a flow rate of 1.0 mL min^{-1}. BPA was monitored at a detection wavelength of 278 nm.

2.2. Synthesis of Water-Dispersible Molecularly Imprinted Polymers (MIPs)

Water-dispersible molecularly imprinted polymers (MIPs) were synthesized according to the literature with some modifications [25]. The specific procedure was as follows. BPA (1 mmol), AMPS (2.5 mmol), and St (2.5 mmol) were sequentially dissolved in DMF (20 mL) and stirred to form a pre-polymerization solution. After purging the pre-polymerization solution with nitrogen gas for 20 min, the crosslinker EGDMA (1.88 mL) and the initiator AIBN (35 mg) were added to the solution. The mixture was first subjected to ultrasonication for 15 min and subsequently stirred at room temperature for 6 h. The polymerization process was carried out in a water bath at 50 °C for 24 h. Finally, the obtained MIPs were collected and eluted with an ethanol: acetic acid (9:1, *v*/*v*) solution to remove the template molecules. The completeness of the template removal was monitored by UV-Vis spectrophotometry, checking for the absence of the BPA peak at 278 nm. Residual acetic acid was washed away with ethanol. The MIPs were vacuum-dried at 60 °C, then ground and stored sealed at room temperature for further use. Non-imprinted polymers (NIPs) were prepared using the same process, except that the template molecule BPA was absent from the pre-polymerization solution.

2.3. Preparation of the Semi-Interpenetrating N/C Hydrogel Precursor

NIPAM (1.55 g) and a certain amount of CMCS were dissolved in deionized water (17 mL). After mixing uniformly, the crosslinker MBA (25.344 mg) and the accelerator TEMED (50 μL) were added. The obtained NIPAM/CMCS(N/C) precursor solution was ultrasonicated for 15 min and then stored at room temperature, protected from light for further use.

2.4. Preparation of the Molecularly Imprinted Polymers Incorporated Semi-Interpenetrating Network

The hydrogel precursor solution (2 mL) was mixed with a certain amount of water-dispersible MIPs powder. After stirring evenly, the initiator ammonium persulfate (200 μL, 0.08 g/mL) was added to the solution with stirring. The precursor solution was injected into a mold, and the excess on the surface was scraped off to achieve a gel membrane with the thickness of 1 mm. It was left to stand at room temperature for 24 h to obtain the MIPs incorporated semi-interpenetrating network gel membrane $MIP_x@N/C_y$ (where x is the incorporated MIPs concentration in g/mL and y is the mass concentration of CMCS in the precursor in wt%). The gel membrane was removed and immersed in deionized water for 24 h, changing the water every 8 h, to wash away unreacted monomers from the network. The cleaned membrane was freeze-dried for further use.

2.5. Adsorption Studies

The adsorption performance of $MIP_x@N/C_y$ membranes was investigated through both equilibrium and time-dependent adsorption assays. Membrane samples (1 cm × 1 cm) were placed in 3 mL of BPA solution prepared in a methanol/water solvent system (1:9, *v*/*v*) with different initial analyte concentrations. To evaluate adsorption isotherms, BPA concentrations were varied from 5.0 to 230.0 mg/L, and the adsorption process was conducted for 24 h at three temperatures (15, 25, and 35 °C). Time-resolved adsorption experiments were performed using a BPA concentration of 50 mg/L at predetermined contact times. Following adsorption, the membranes were removed from the solution, and the remaining BPA concentration was quantified by UV–vis spectroscopy at 278 nm. The equilibrium adsorption data were interpreted using the Langmuir and Freundlich models, whereas adsorption kinetics were examined through pseudo-first-order and pseudo-second-order kinetic equations.

The following Equation (1) was used for the calculation of the BPA equilibrium adsorption capacity (Q_e, mg/g) on the membrane [26]:

$$Q_e = \frac{(C_0 - C_e) \times V}{m} \tag{1}$$

where C_0 and C_e (mg/L) denote the BPA concentrations before and after adsorption equilibrium, respectively. V (L) represents the solution volume, and m (g) refers to the membrane mass.

Adsorption kinetics were further assessed under conditions comparable to those used in the equilibrium study. Specifically, membrane samples were incubated in 3 mL BPA solution (150 mg/L) at ambient temperature for contact times spanning 5–800 min. During adsorption, the BPA concentration at each sampling time (C_t, mg/L) was monitored using UV–vis spectroscopic analysis. The adsorption capacity at a given time point (Q_t, mg/g) was estimated using Equation (2) [27]:

$$Q_t = \frac{(C_0 - C_t) \times V}{m} \tag{2}$$

The resulting kinetic data were fitted using the pseudo-first-order and pseudo-second-order kinetic models. In addition, adsorption equilibrium data obtained from isotherm experiments were analyzed with the Langmuir and Freundlich models to better elucidate the adsorption characteristics of the prepared membranes.

2.6. Selective Adsorption Performance and Regeneration Efficiency

For selectivity analysis, $MIP_x@N/C_y$ membranes (1 cm × 1 cm) were immersed in 3 mL of a mixed solvent composed of methanol and water (1:9, *v*/*v*) containing various interferences. Adsorption was conducted at 25 °C for 24 h. After equilibration, the concentrations of analogues remaining in the supernatant were quantified. The Equation (3) was used to study the selectivity factor (a) of the $MIP_x@N/C_y$ membrane [28]:

$$\alpha = RE_{\text{template}}/RE_{\text{analogue}} \tag{3}$$

where RE_{template} and RE_{analogue} denote the removal efficiency of the template molecule and its competing analogue. The removal efficiency (RE) was determined by Equation (4) [29]:

$$RE = \frac{C_{\text{initial}} - C_{\text{equilibrium}}}{C_{\text{initial}}} \times 100\% \quad (4)$$

In this equation, C_{initial} corresponds to the initial concentration of the analyte, whereas $C_{\text{equilibrium}}$ represents its equilibrium concentration after adsorption. Reusability was investigated through repeated adsorption–desorption procedures. Following each rebinding experiment, the membranes were washed with an ethanol/water solution (9:1, *v*/*v*) until BPA was no longer detectable in the eluent. The regenerated samples were subsequently reused for adsorption testing over six consecutive cycles, and the BPA uptake performance of MIP@N/C was recorded after every regeneration step.

2.7. Thermodynamic Studies

The thermodynamic parameters characteristics of BPA adsorption onto MIP@N/C were evaluated according to the adsorption equilibrium data. The corresponding parameters, including Gibbs free energy change (ΔG), enthalpy change (ΔH), and entropy change (ΔS) f were determined following established thermodynamic equations (Equations (5)–(7)) [30]:

$$\ln K = -\Delta G/RT \quad (5)$$

$$\Delta G = \Delta H - T\Delta S \quad (6)$$

$$\ln K = \Delta S/R - \Delta H/RT \quad (7)$$

where K denotes the adsorption equilibrium constant reflecting the interaction affinity between adsorbent and adsorbate, while R and T correspond to the universal gas constant and absolute temperature. The value of ΔG was estimated from the linear relationship between $\ln K$ ($K = Q_e/C_e$) and $1/RT$ based on Equation (5).

2.8. Application of MIP$_x$@N/C$_y$ for the Removal of BPA in Water Samples

Considering the typically low concentration of BPA pollutants in daily water samples, it was presumed that the water samples themselves might not contain BPA. However, the plastic packaging materials holding water could potentially release BPA into water under high temperatures. To simulate the release process of BPA from packaging plastics into water, 1100 mL of purified water was heated together with a takeaway container (PP), a plastic water bottle (PET), and a PC plastic barrel (PC) at 120 °C for 3 h, respectively, and then evaporated at 95 °C to concentrate to a final volume of 10 mL, thus obtaining concentrated and enriched water samples containing BPA for testing. A piece of MIPx@N/Cy membrane was immersed in 3 mL of the enriched water sample for adsorption, followed by elution with 1 mL of methanol. The concentrated water samples before and after adsorption by the MIPx@N/Cy membrane, along with the elution solution, were analyzed by HPLC to verify the feasibility of the prepared MIP@N/C for BPA accumulation and removal.

To further evaluate the performance of MIP$_{0.06}$@N/C$_3$% under realistic conditions, a real industrial wastewater sample was collected from the production process of Jiangsu Yangnong Chemical Group Co., Ltd. (Yangzhou, China). This wastewater contains BPA as one of the major organic pollutants, along with various inorganic salts and organic byproducts. The raw wastewater was first filtered through a 0.45 μm membrane to remove suspended solids, and its initial BPA concentration was determined by UV-vis to be 9.7 mg/L (mean value of triplicate measurements). No additional BPA was spiked. A piece of MIP$_{0.06}$@N/C$_3$% membrane (1 cm × 1 cm) was immersed in 3 mL of the filtered wastewater and allowed to adsorb for 8 h at room temperature under shaking (150 rpm). After adsorption, the residual BPA concentration in the wastewater was analyzed by HPLC. The removal efficiency was calculated according to Equation (4). Three parallel experiments were conducted to ensure reproducibility.

3. Results and Discussion

3.1. Optimization of MIP$_x$@N/C$_y$ Preparation and Their Characterizations

To enhance the hydrophilicity of molecularly imprinted polymers (MIPs), the hydrophilic monomer 2-acrylamido-2-methylpropanesulfonic acid (AMPS) was introduced as a functional monomer. Dynamic water contact angle (WCA) measurements (Figure 2) revealed that MIPs synthesized using AMPS (Figure 2B) exhibited strong hydrophilic characteristics: the contact angle was only 24.67° at 0.1 s and dropped rapidly to complete spreading within 5 s. In contrast, MIPs prepared with methacrylic acid (MAA) as the functional monomer (Figure 2A) showed slower water spreading, with the contact angle decreasing from 50.53° at 0.1 s to 34.32° at 5 s. These results demonstrate that the incorporation of AMPS significantly improves the surface hydrophilicity of the MIPs.

To further evaluate whether this enhanced hydrophilicity translates into better adsorption performance, we compared the BPA adsorption capacities of AMPS-based and MAA-based MIPs under identical conditions (Figure 2C). The results showed that the adsorption capacity of hydrophilic AMPS-MIP@N/C membrane reached 113.66 mg/g, whereas that of hydrophobic MAA-MIPs@N/C membrane was only 80.24 mg/g under the same conditions.

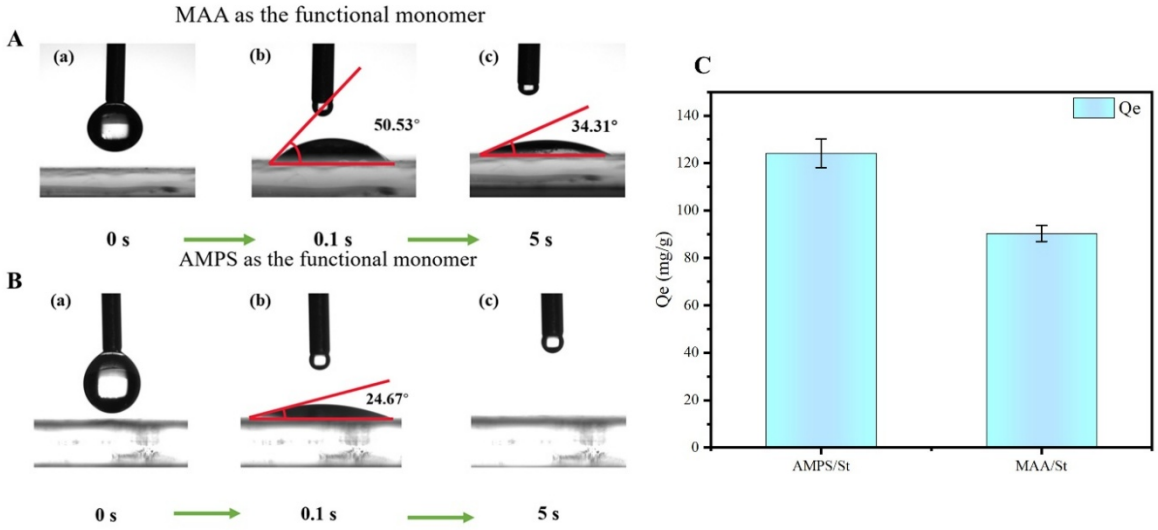

Figure 2. Dynamic WCA images of MIPs prepared using MAA (**A**) and AMPS (**B**) as functional monomers within 0–5 s. (**C**) Comparison of BPA adsorption capacity of MIP@N/C membranes prepared with AMPS-based (hydrophilic) and MAA-based (hydrophobic) MIPs.

The adsorption capacity of $MIP_x@N/C_y$ is strongly influenced by both the network structure of the hydrogel and the number of incorporated MIPs. CMCS, as a component of the semi-interpenetrating network, plays a role in regulating pore architecture and network looseness of $MIP_x@N/C_y$, thereby affecting the accessibility of target molecules to imprinted binding sites. Selecting an appropriate CMCS concentration favors the adsorption process. As shown in Figure 3A, the adsorption performance was increased when the CMCS concentration was increased from 1 wt% to 3 wt% and reached a maximum at 3 wt%. This indicated that, at this concentration, the hydrogel network forms an optimal porous structure that that facilitates BPA diffusion and binding. However, further increasing CMCS to 3.5 wt% reduces adsorption capacity. This decline is likely due to excessive polymer content causing a denser network structure, which restricts mass transfer and limits access to recognition sites. MIPs possess cavities that can specifically adsorb BPA, and their content directly affects the adsorption performance of $MIP_x@N/C_y$. Figure 3B indicated that the adsorption effect was best when the contents of MIPs blended in the hydrogel precursor solution was 0.06 g/mL where the highest Q_e was observed. This improvement is attributed to the greater number of specific recognition cavities introduced by the MIPs. However, when the MIP concentration exceeds 0.06 g mL^{-1}, adsorption performance declines sharply. This reduction can be explained by the dual role of nanoparticles in the hydrogel system. Besides providing specific binding sites, MIPs act as multifunctional crosslinking and reinforcing nodes through hydrogen bonding and interfacial interactions with polymer chains. At excessive loadings, nanoparticle aggregation occurs, leading to structural heterogeneity, increased crosslink density, and partial blockage of pores and imprinted cavities. These effects hinder BPA diffusion and reduce the effective number of accessible binding sites [31,32]. Therefore, subsequent experiments selected a CMCS concentration of 3 wt% and an MIPs concentration of 0.06 g/mL ($MIP_{0.06}@N/C_{3\%}$).

The effects of CMCS and MIPs concentrations on the membrane morphology were also investigated. Figure 4A–C show the surface morphologies of the hydrogel membranes prepared at different CMCS concentrations. All the membranes display honeycomb-like porous structure with interconnected pore networks. As the CMCS concentration increases from 1% to 3%, a progressive morphological transition is observed: the average pore diameter decreases significantly while the pore density increases, resulting in a more compact and denser matrix structure. This structural evolution arises from the increased viscosity of the precursor solution at higher CMCS concentrations and the enhanced crosslinking density between CMCS carboxyl groups and NIPAM amide functionalities, which restricts phase separation during polymerization. These factors drive the formation of a denser hydrogel framework with smaller pores. Pore size has an important influence on the adsorption performance. Generally, an appropriate porous structure can facilitate the diffusion and transport of target

molecules, thereby enhancing their accessibility to imprinted recognition sites. According to previous studies on porous adsorbents, larger pores are beneficial for mass transfer, whereas excessively small pores may hinder the diffusion of BPA molecules into the internal binding sites. In contrast, overly large pores may reduce the specific surface area and decrease the density of effective recognition sites. Therefore, an optimal pore structure is required to balance mass transfer efficiency and the availability of binding sites. Based on structural integrity and porosity optimization, a CMCS concentration of 3% was selected for subsequent experiments. The incorporation of MIP particles introduces additional macropores and creates a rougher surface topology due to the rigid MIP scaffold disrupting the regular polymer network formation. The MIPs distributed within the hydrogel membrane provide numerous specific adsorption sites for BPA. Additionally, they strengthen the membrane's structural stability, leading to improved stability in water, suppressed swelling, and prevention of rupture caused by excessive water absorption However, excessive MIPs loading results in particle aggregation within the pore channels (Figure 4D), causing pore blockage and reduced mass transfer efficiency. Therefore, the optimal membrane was obtained with CMCS mass concentration of 3% and MIP concentration of 0.06 g/mL, designated as $MIP_{0.06}@N/C_{3\%}$. This membrane maintains an open, interconnected porous structure that balances mechanical stability with rapid analyte diffusion.

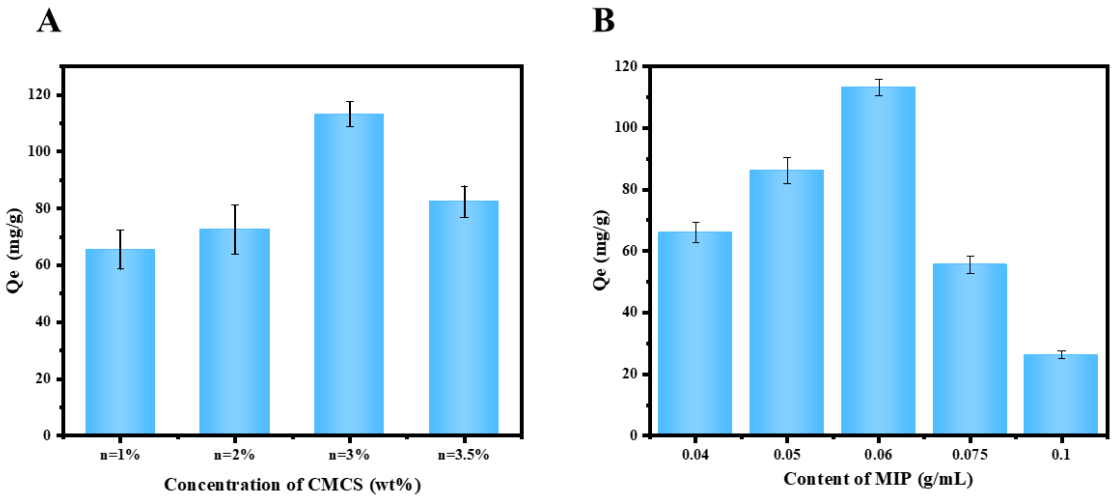

Figure 3. Effect of (**A**) CMCS concentration and (**B**) MIPs contents on the adsorption capacity of MIP@N/C.

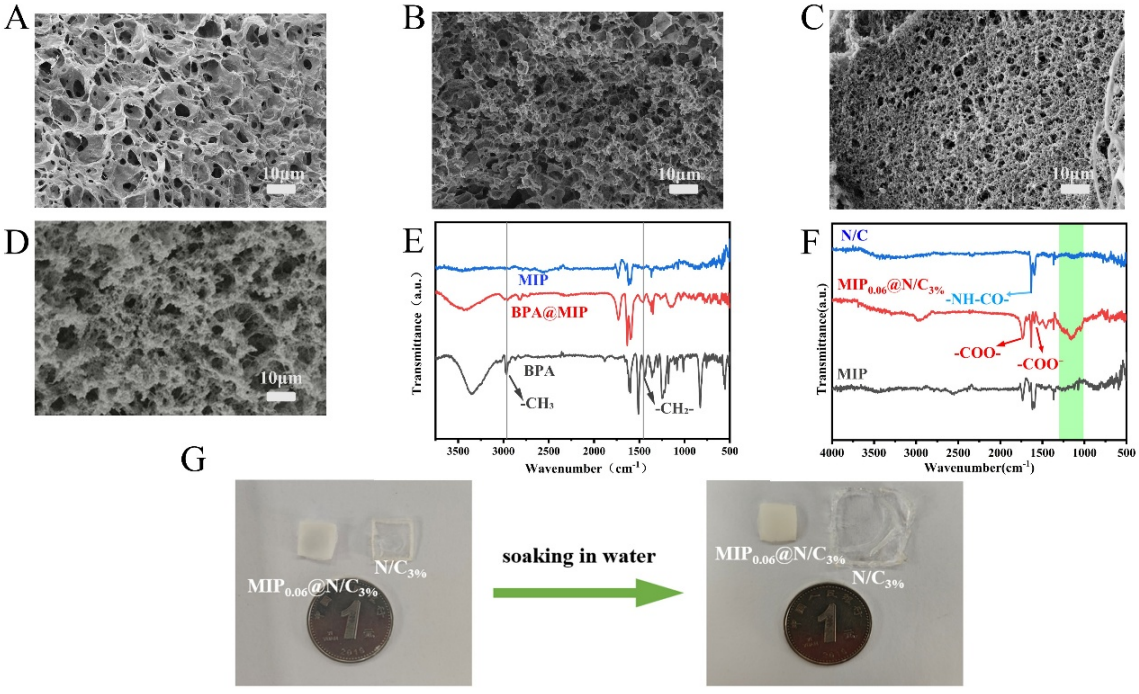

Figure 4. SEM images of (**A**) $MIP_{0.06}@N/C_{1\%}$; (**B**) $MIP_{0.06}@N/C_{2\%}$; (**C**) $MIP_{0.06}@N/C_{3\%}$; (**D**) $MIP_{0.1}@N/C_{3\%}$; FT-IR spectra of (**E**) MIP; BPA@MIP and BPA and (**F**) MIP, N/C and $MIP_{0.06}@N/C_{3\%}$; Photographs of (**G**) $MIP_{0.06}@N/C_{3\%}$ and $N/C_{3\%}$ before and after soaking in water.

The chemical compositions and template elution were characterized using FT-IR. Figure 4E shows the infrared spectra of pristine MIP (after template removal), and MIP loaded with BPA (MIP@BPA), and BPA. Compared to MIP, the most significant difference in the spectra of MIP@BPA and BPA is the appearance of a distinct absorption peak at 2974 cm^{-1} when BPA is present, which is attributed to the C-H stretching vibrations of the two methyl groups in the central isopropyl moiety of BPA [33]. This peak is absent in the MIP spectrum, indicating that the BPA template molecules have been successfully eluted from the polymer matrix, leaving cavities capable of specific recognition of BPA. Figure 4F shows the FT-IR spectra of MIP, NIPAM/CMCS (N/C), and $MIP_{0.06}$@$N/C_{3\%}$. Following the incorporation of MIPs into the N/C hydrogel, a C=O stretching vibration peak appears at 1732 cm^{-1}, corresponding to the ester groups (-COOR-) in the MIP. The hydrogel's characteristic peaks at 1592 cm^{-1} (carboxylate, COO^-) and 1632 cm^{-1} (secondary amide, -NH-CO-) persist, indicating successful incorporation of MIP into the hydrogel membrane. After MIP addition, a broad absorption band emerges in the range of 1010–1300 cm^{-1}. This broadness likely arises from interfacial interactions between the MIP and the hydrogel network, where functional groups from both components interact. Simultaneously, hydrophobic interactions between the MIP's benzene rings (styrene moieties) and PNIPAM's isopropyl groups may perturb the hydrogen-bond network. The concerted action of these interactions yields the broad band in this region, suggesting the MIP and hydrogel have established a new hydrogen-bonded network rather than existing as a simple physical blend [34]. The macroscopic swelling behavior of the membranes is illustrated in Figure 4G. Digital photographs show that the $MIP_{0.06}$@$N/C_{3\%}$ membrane exhibited reduced swelling (left) compared to the pristine N/C membrane (right) after immersion in water. The pristine hydrogel swells excessively, becoming translucent and mechanically fragile, whereas the MIP-loaded membrane maintains its structural integrity, opacity, and dimensional stability. This suppressed swelling behavior confirms that the MIP incorporation establishes a more rigid, physically crosslinked network structure that resists hydrophilic expansion, preventing the rupture of imprinted cavities and maintaining stable recognition sites during aqueous operation.

Based on the above characterizations, the distinct functions of the two components can be summarized. The MIP particles, uniformly dispersed within the hydrogel matrix, provide the specific recognition cavities for BPA. The successful imprinting is evidenced by the FTIR peak at 2974 cm^{-1} (Figure 4E) that appears only after BPA rebinding, and the enhanced adsorption capacity of MIP@N/C compared to NIP@N/C. Meanwhile, the N/C semi-IPN hydrogel plays multiple roles. First, its honeycomb-like porous structure (Figure 4C) with interconnected pores acts as a low-resistance transport channel for BPA, ensuring rapid diffusion to the imprinted sites. Second, the hydrophilic nature of the N/C network, derived from the amide and carboxyl groups, prevents excessive aggregation of the hydrophobic MIP domains and maintains a hydrated environment favorable for hydrogen-bonding interactions. Third, the crosslinked NIPAM/CMCS network physically confines the MIP particles, suppressing their aggregation and leaching, and enhances the mechanical integrity of the composite membrane, as reflected by the reduced swelling ratio (Figure 4G). Consequently, the N/C matrix not only supports the MIP but also actively contributes to non-specific adsorption and mass transfer, synergistically boosting the overall performance.

Mechanical properties of the hydrogel membranes were evaluated by uniaxial tensile testing. As shown in Figure 5, the pure N/C hydrogel exhibited a tensile strength of 0.046 MPa, an elongation at break of 32.6%, a Young's modulus of 0.48 MPa, and a toughness of 26.7 kJ/m^3. In contrast, the $MIP_{0.06}$@$N/C_{3\%}$ membrane showed significantly enhanced mechanical performance, with a tensile strength of 0.214 MPa, an elongation at break of 90.4%, a Young's modulus of 0.85 MPa, and a toughness of 114 kJ/m^3. The substantial improvement is attributed to the formation of an interfacial hydrogen-bonding network between the hydrophilic MIPs and the N/C hydrogel matrix, which acts as physical crosslinking nodes and suppresses excessive swelling, thereby reinforcing the network structure. These results confirm that the incorporation of MIPs not only provides specific recognition sites but also effectively strengthens the mechanical integrity of the hydrogel membrane, which is critical for the practical application of the material.

The porosity of the $MIP_{0.06}$@N/C_3% membrane was characterized by nitrogen adsorption–desorption measurements (Figure 6A). The isotherm exhibits a type I/IV hybrid shape with a distinct H3-type hysteresis loop at high relative pressures ($P/P_0 > 0.8$), indicating the coexistence of micropores and mesopores. The steep N_2 uptake at very low ($P/P_0 < 0.01$) is characteristic of micropore filling, while the gradual increase in the intermediate P/P_0 range (0.1–0.8) and the hysteresis loop are typical of capillary condensation within mesopores. The BET specific surface area calculated from the linear region ($P/P_0 = 0.05–0.30$) is 100.0 m^2/g, and the total pore volume at $P/P_0 = 0.989$ is 0.282 cm^3/g. The pore size distribution (inset of Figure 6A) obtained from the BJH adsorption branch shows a broad mesopore peak centered at approximately 4.2 nm, with a mesopore volume of 0.277 cm^3/g. In addition, the HK micropore size distribution (Figure 6B) reveals a primary micropore width of 0.83 nm with a micropore volume of 0.026 cm^3/g, which is consistent with the molecular dimension of BPA and supports the specific recognition function of the imprinted cavities. The distribution also displays some fine structures beyond

1.0 nm, possibly arising from the presence of additional small pores within the semi-IPN hydrogel matrix or from minor deviations due to the model assumptions of the HK method.

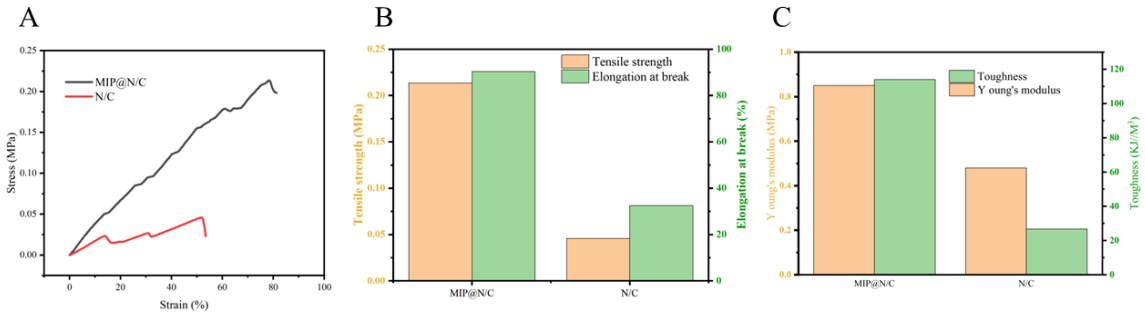

Figure 5. (**A**) Tensile stress–strain curves of the pristine N/C hydrogel and the $MIP_{0.06}$@N/C_3% membrane. (**B**) Comparison of tensile strength and elongation at break. (**C**) Comparison of Young's modulus and toughness.

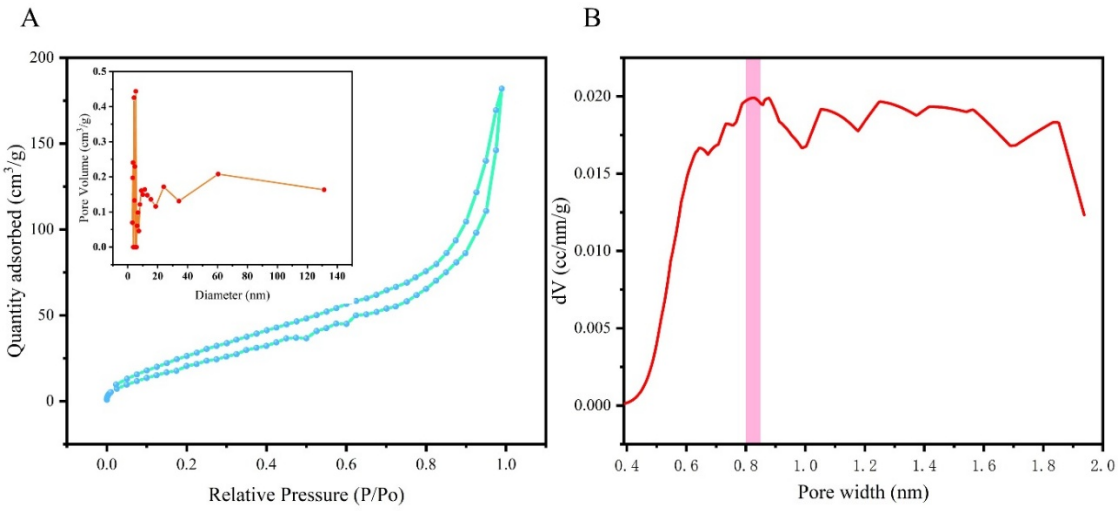

Figure 6. (**A**) Nitrogen adsorption-desorption isotherms and pore size distribution of $MIP_{0.06}$@N/$C_{3\%}$; (**B**) HK micropore size distribution of $MIP_{0.06}$@N/$C_{3\%}$.

3.2. Adsorption Properties of $MIP_{0.06}$@N/$C_{3\%}$

3.2.1. Comparison of Adsorption Performance of Individual Components

To elucidate the respective roles of MIPs and the N/C hydrogel matrix in the composite membrane, we evaluated the BPA adsorption capacity of pure MIP particles (without hydrogel) and pure N/C hydrogel membrane (without MIP) under identical conditions (initial BPA concentration = 230 mg/L, 25 °C, 24 h). As shown in Table 1, the pure MIP particles exhibited an equilibrium adsorption capacity of 124.14 mg/g, but suffered from severe aggregation in aqueous solution and difficulty in separation. The pure N/C hydrogel membrane showed a capacity of 52.91 mg/g, which is attributed to non-specific adsorption through hydrogen bonding and hydrophobic interactions provided by the NIPAM/CMCS network. In contrast, the MIP@N/C composite membrane achieved a significantly higher capacity of 113.66 mg/g under the same conditions. MIP component supplies specific recognition cavities for BPA, while the N/C hydrogel matrix not only prevents MIP aggregation and ensures good dispersion but also facilitates mass transfer and provides additional non-specific binding sites. The combination of specific and non-specific interactions, together with the porous semi-IPN structure, accounts for the superior adsorption performance of MIP@N/C.

Table 1. Maximum adsorption capacity at different temperatures.

Q_m (mg/g)	298 K
$MIP_{0.06}$@N/$C_{3\%}$	113.66
N/$C_{3\%}$	52.91
MIP	124.14

3.2.2. Adsorption Isotherms and Kinetics

Isothermal adsorption of BPA on $MIP_{0.06}$@$N/C_{3\%}$ was measured at 288 K, 298 K, and 308 K. The adsorption results were fitted using the Langmuir and Freundlich models, respectively. The fitting curves are shown in Figure 7A,B. The isothermal adsorption model parameters calculated from the formulas are listed in Table 2. Although the R^2 of the Langmuir model at 288 K was slightly greater than that of the Freundlich model, the Langmuir model fit poorly at 308 K, whereas the R^2 for the Freundlich model remained more consistent. This suggests that the Freundlich model better describes BPA adsorption and suggesting multilayer adsorption.

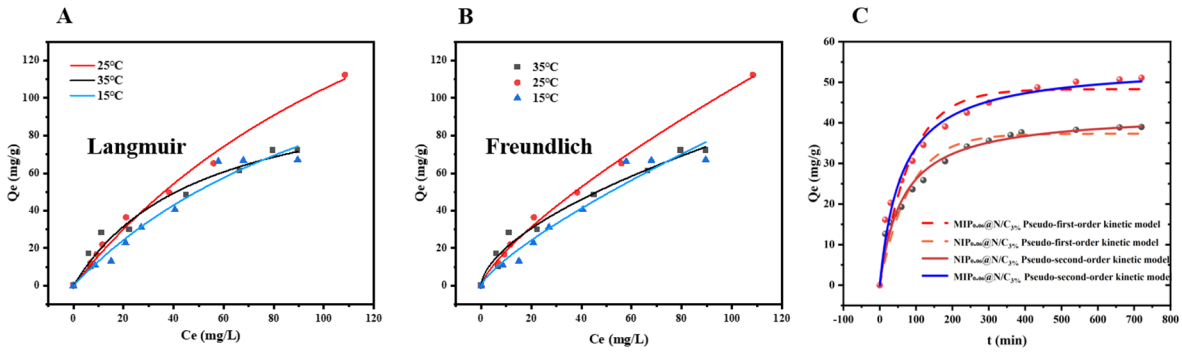

Figure 7. (**A**) The Langmuir model at 15 °C, 25 °C and 35 °C; (**B**) The Freundlich model at 15 °C, 25 °C and 35 °C; (**C**) Adsorption kinetics: Pseudo-first-order model and Pseudo-second-order model of $MIP_{0.06}$@$N/C_{3\%}$ and $NIP_{0.06}$@$N/C_{3\%}$ for BPA adsorption.

Table 2. Isothermal adsorption model parameters.

Adsorbate	Model	Parameter	Temperature (K)		
			288	298	308
BPA	Freundlich	K_f	0.872	3.275	4.974
		n	0.942	1.328	1.654
		R^2	0.986	0.996	0.974
	Langmuir	Q_e	66.210	113.66	61.341
		K_L	0.021	0.006	0.020
		R^2	0.998	0.986	0.942

To study and verify the time-dependent adsorption behavior of $MIP_{0.06}$@$N/C_{3\%}$, the adsorption kinetics experiments were performed at an initial BPA concentration of 150 mg/L, with parallel adsorption tests on $NIP_{0.06}$@$N/C_{3\%}$ for comparison. The results were fitted using the pseudo-first-order and pseudo-second-order kinetic models, and the fitting curves are shown in Figure 7C. The calculated relevant kinetic parameters are listed in Table 3. Throughout the time range, the adsorption capacity of $MIP_{0.06}$@$N/C_{3\%}$ was greater than that of $NIP_{0.06}$@$N/C_{3\%}$. The adsorption of BPA by $MIP_{0.06}$@$N/C_{3\%}$ increased rapidly within the first 60 min and approached equilibrium around 4 h. The Q_t of $NIP_{0.06}$@$N/C_{3\%}$ showed a similar trend over time, but the final adsorption capacity was lower. A possible explanation for this phenomenon is that the presence of imprinted cavities in $MIP_{0.06}$@$N/C_{3\%}$ enhances its ability to precisely recognize BPA. The lower adsorption capacity of $NIP_{0.06}$@$N/C_{3\%}$ compared to $MIP_{0.06}$@$N/C_{3\%}$ is due to the lack of adsorption sites capable of specifically recognizing BPA in the NIP. However, since the hydrogel itself also has a certain capacity to adsorb BPA, $NIP_{0.06}$@$N/C_{3\%}$ still shows adsorption for BPA, but with a lower adsorption capacity than $MIP_{0.06}$@$N/C_{3\%}$.

Table 3. Kinetic fitting data of BPA binding by different membranes.

Absorbents	Pseudo-First-Order-Kinetics $\ln(Q_e - Q_t) = \ln Q_e - k_1 t$			Pseudo-Second-Order-Kinetics $Q_t = (k_2 Q_e^2 t)/(1 + k_2 Q_e t)$		
	Q_e (mg/g)	K_1 (L/mg)	R^2	Q_e (mg/g)	K_2 (g/mg/min)	R^2
$MIP_{0.06}$@$N/C_{3\%}$	48.311	0.012	0.944	54.441	3.034×10^{-4}	0.982
$NIP_{0.06}$@$N/C_{3\%}$	35.813	0.014	0.946	42.471	3.761×10^{-4}	0.974

3.2.3. Adsorption Thermodynamics

Based on the isothermal adsorption study, the data were processed and fitted. The thermodynamic parameters were calculated from the equilibrium constants using Equations (5)–(7), and they are listed in Table 4.

Table 4. Thermodynamic adsorption parameters of for $MIP_{0.06}@N/C_{3\%}$ for BPA.

Adsorbate	Temperature (K)	Δ*G* (kJ/mol)	Δ*H* (kJ/mol)	Δ*S* (J/mol/K)
BPA	288	−0.347	14.831	52.536
	298	−0.725		
	308	−1.404		

Table 4 shows that the Δ*G* for the entire adsorption process is small, indicating that the adsorption reaction is reversible. The absolute value of Δ*G* gradually increases with the increasement of the temperature. This is because, as the temperature increases, the hydrogen bonds formed between the amide groups and water gradually transform into interactions between the amide groups themselves [35,36], and the association between hydrophobic isopropyl groups enhances. The hydrophobicity of the hydrogel increases, and its affinity for BPA also improves. As shown in Table 5, the adsorption capacity at 298 K (113.66 mg/g) is higher than that at 288 K (66.21 mg/g). However, when the temperature continues to rise to 308 K, the adsorption capacity decreases. This is because 308 K is above the lower critical solution temperature (LCST) of the NIPAM gel, causing changes in the long-chain structure of the gel polymer. Spatial contraction makes it difficult for the adsorption sites to bind with BPA, hence the decrease in adsorption capacity at 308 K, with the maximum adsorption capacity observed at 298 K.

Table 5. Maximum adsorption capacity at different temperatures.

Q_m (mg/g)	288 K	298 K	308 K
$MIP_{0.06}@N/C_{3\%}$	66.21	113.66	72.14
$NIP_{0.06}@N/C_{3\%}$	34.55	52.87	45.32

3.2.4. Adsorption Mechanism of MIP@N/C for BPA

The excellent adsorption performance of MIP@N/C (113.66 mg/g) arises from a combination of specific recognition, non-specific interactions, and structural synergy. The imprinted cavities formed during polymerization are complementary to BPA in size, shape and functional group arrangement. Upon rebinding, the phenolic –OH groups of BPA form hydrogen bonds with the sulfonic acid groups of AMPS and the amide groups of the MIP matrix, while the styrene units provide a hydrophobic microenvironment that enhances π–π stacking with the bisphenyl rings of BPA. FTIR evidence (Figure 4E) shows a distinct peak at 2974 cm^{-1} in the MIP@BPA spectrum, corresponding to the C–H stretching of the two methyl groups of BPA, confirming successful capture. In parallel, the PNIPAM/CMCS network offers abundant amide, carboxyl and isopropyl groups, which interact with BPA through hydrogen bonding and hydrophobic interactions, respectively. The pure N/C membrane alone exhibited a capacity of 52.9 mg/g (Table 1), confirming the contribution of non-specific binding. Moreover, the honeycomb-like porous structure (SEM, Figure 4C) facilitates rapid mass transfer and provides accessible sites. Importantly, the MIP and N/C components are not simply physically mixed. The FTIR spectrum of MIP@N/C (Figure 4F) shows a broad band at 1010–1300 cm^{-1}, absent in both pure MIP and pure N/C, indicating the formation of an interfacial hydrogen-bonding network between the sulfonic/ester groups of MIP and the amide/carboxyl groups of N/C. This network not only prevents MIP aggregation but also enhances mechanical strength and suppresses excessive swelling (Figure 4G), thereby protecting the imprinted cavities from deformation in aqueous media. The adsorption data follow the Freundlich isotherm (R^2 = 0.986–0.996), suggesting multilayer adsorption on a heterogeneous surface-a finding that directly reflects the coexistence of specific imprinted sites and non-specific hydrogen bonding/hydrophobic interactions. The pseudo-second-order kinetic model (R^2 = 0.982) indicates that chemisorption (hydrogen bonding and hydrophobic interactions) is the rate-limiting step, rather than simple diffusion. Thermodynamic parameters provide further insight: ΔH = +14.83 kJ/mol (endothermic), ΔS = +52.54 J/mol·K (positive), and $\Delta G < 0$ (spontaneous). The positive ΔH indicates an endothermic adsorption process, which is primarily attributed to the hydrophobic interactions between BPA and the polymer network as well as the dehydration of the imprinted cavities upon binding. Meanwhile, the positive ΔS arises from the displacement of hydrated water molecules from the cavities, increasing the system's disorder. Together, these thermodynamic parameters confirm an endothermic, entropy-driven adsorption process that is fully consistent with the proposed molecular-level interactions. Taken together, the high adsorption capacity of MIP@N/C

is the result of synergistic contributions from specific cavity recognition, hydrogen bonding, hydrophobic effects, and a porous semi-IPN hydrogel structure that ensures good accessibility and fast mass transfer.

In practical water treatment scenarios, flow-through operation is often preferred over static batch adsorption due to its higher throughput and compatibility with continuous monitoring. Although the current study was conducted under static conditions owing to the lack of an appropriate flow system in our laboratory, a mechanistic discussion on the expected behavior of MIP@N/C under flow is warranted.

Under laminar or moderate flow conditions, enhanced convective mass transport is expected to reduce the diffusion boundary layer thickness around the hydrogel membrane, thereby accelerating analyte transport to the imprinted recognition sites. This would likely improve the adsorption kinetics and shorten the response time compared to static incubation. Since the binding in our MIP@N/C system is governed by specific affinity cavities rather than purely diffusion-limited accumulation, moderate flow rates (e.g., 0.5–2.0 mL/min for a membrane reactor configuration) are not anticipated to significantly compromise the equilibrium binding capacity. On the contrary, a moderate increase in flow rate may enhance the utilization of surface-accessible imprinted sites by mitigating boundary layer effects.

However, at excessively high flow rates, the residence time of the analyte solution within the membrane may become too short for sufficient interaction between BPA and the imprinted cavities, leading to a decrease in apparent adsorption capacity. Such trade-off between flow rate and binding efficiency has been widely documented for molecularly imprinted membranes and other affinity-based adsorbents [38,39]. Additionally, the excellent mechanical strength and suppressed swelling of $MIP_{0.06}$@N/C_3% (Figures 4G and 5) suggest that the membrane can withstand moderate hydraulic pressures without structural deformation or loss of imprinted sites. Therefore, we anticipate that the MIP@N/C membrane is well-suited for flow-through applications, provided that the flow rate is optimized to balance mass transfer enhancement and sufficient analyte–receptor contact time. Future work will focus on integrating this membrane into a continuous flow cell to validate these predictions and evaluate long-term operational stability.

3.3. Reusability and Selectivity of $MIP_{0.06}$@N/$C_{3\%}$

Adsorption-desorption experiments were conducted on $MIP_{0.06}$@N/$C_{3\%}$, using an ethanol/water (*v*:*v* = 9:1) mixture as the desorption solution. Due to the "co-nonsolvency" phenomenon [37] exhibited by NIPAM in the hydrogel membrane within the ethanol/water mixture, although both water and ethanol are good solvents for NIPAM, when ethanol and water coexist, the solvent molecules disrupt the hydrogen bonds between the amide groups and the solvent. The affinity between ethanol and water molecules is greater than the affinity between the polymer segments and water molecules or between the segments and ethanol molecules, leading to the "co-nonsolvency" phenomenon. This causes the polymer network to collapse, thereby rapidly eluting the BPA bound within the hydrogel network. As shown in Figure 8A, the removal efficiency remained above 99% after six cycles, and even after ten and twelve cycles it still reached 98.27% and 97.73%, respectively. These results demonstrate the outstanding reusability of the prepared $MIP_{0.06}$@N/C_3% over at least twelve consecutive adsorption–desorption cycles.

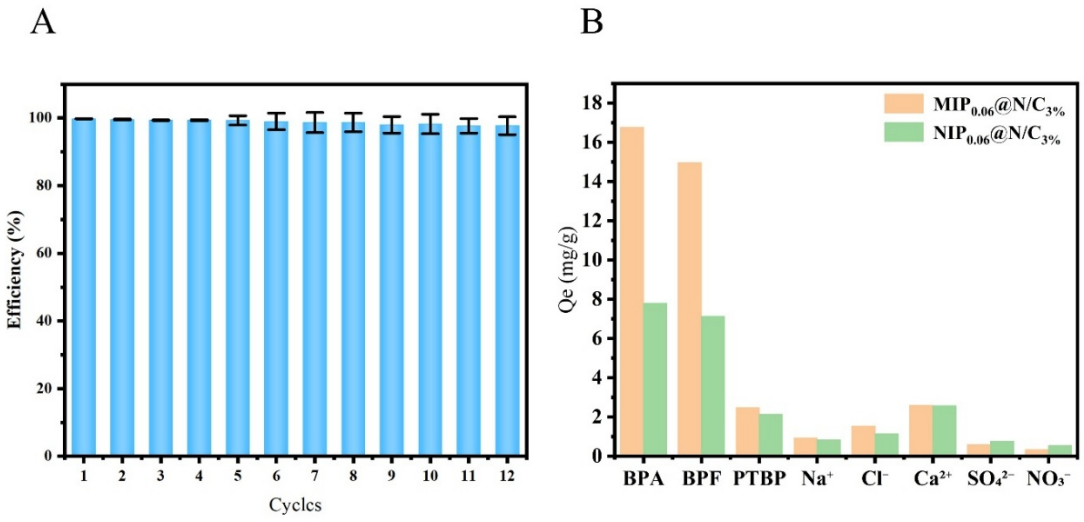

Figure 8. (**A**) Adsorption efficiency of $MIP_{0.06}$@N/$C_{3\%}$ during twelve consecutive regeneration cycles; (**B**) Removal efficiency of $MIP_{0.06}$@N/$C_{3\%}$ and $NIP_{0.06}$@N/$C_{3\%}$ toward BPA, BPF, and PTBP, some common cations and ions (Ca^{2+}, Cl^-, SO_4^{2-}, Na^+, NO_3^-) individually.

The adsorption selectivity of $MIP_{0.06}@N/C_{3\%}$ for BPA structural analogs, p-tert-butylphenol and bisphenol F, was investigated. The concentrations of BPA and its structural analogs in the experiment were all 50 mg/L. The experimental results are shown in Figure 8B. The removal efficiencies of $MIP_{0.06}@N/C_{3\%}$ for BPA, BPF, and p-tert-butylphenol were 86.86%, 76.53%, and 9.57%, respectively, with corresponding selectivity factors (α) of 1.13 and 9.07. BPF has a similar structure to BPA, so $MIP_{0.06}@N/C_{3\%}$ also exhibits similar adsorption performance for BPF. However, the presence of specific binding sites results in a higher adsorption capacity for BPA. PTBP has a smaller molecular structure than BPA., leading to a lower adsorption capacity. This indicates that the unique recognition sites in $MIP_{0.06}@N/C_{3\%}$ confer selective adsorption characteristics for BPA and its analogs.

To further evaluate the specificity of $MIP_{0.06}@N/C_{3\%}$ for BPA, the adsorption of the membranes towards five common ions (Ca^{2+}, Cl^{-}, SO_4^{2-}, Na^{+}, and NO_3^{-} with the concentration of 10 mg/L) was investigated. The removal efficiencies for all tested ions were less than 4% (Figure 8B), indicating negligible adsorption of the membrane for these ions. This excellent selectivity toward BPA over both structural analogs and inorganic ions confirms that the imprinted cavities are specifically tailored for the recognition of BPA molecules through size-, shape-, and functional group complementarity.

This work was compared with other published studies using hydrogels as adsorbents for the adsorption and separation of BPA. As can be seen from Table 6, the $MIP_{0.06}@N/C_{3\%}$ gel membrane, compared to gel microspheres, possesses a richer three-dimensional porous network and more adsorption sites. Furthermore, due to the incorporation of MIPs, the $MIP_{0.06}@N/C_{3\%}$ gel membrane exhibits higher selectivity.

Table 6. Adsorption performances of BPA on $MIP_{0.6}@N/C_{3\%}$ in comparison to other references.

Adsorbent	Adsorption Capacity (mg/g)	Cycle Number	Efficiency Retention	Ref.
PVDF@Ag@P@MIMs [a]	33.41	9	72%	[40]
NNM [b]	91.3	5	83%	[41]
CF-MIM [c]	27.81	5	80%	[42]
β-CD-HPAN [d]	45.3	5	55%	[43]
SRt-PAN [e]	17.51	5	73%	[44]
MOF/PAN-MIM [f]	56.63	6	77%	[30]
PES-SiO_2 [g]	55.74	3	95%	[45]
ACF [h]	70.6	3	49%	[46]
$MIP_{0.06}@N/C_{3\%}$	113.66	12	97%	This work

[a] Ag nanoparticle-embedded molecularly imprinted PVDF membrane; [b] Nylon 6,6 nanofibrous membrane; [c] Molecularly imprinted carbon felt; [d] β-Cyclodextrin-modified hydrolyzed polyacrylonitrile membrane; [e] Organic rectorite/polyacrylonitrile composite nanofiber membrane; [f] Metal-organic framework (MOF)/polyacrylonitrile (PAN) hybrid nanofiber membrane; [g] Polyethersulfone (PES)/SiO_2 nanoparticle composite membrane; [h] Activated carbon fiber (ACF) powder composited on polyester (PET) filter clothes.

3.4. Application of $MIP_{0.06}@N/C_{3\%}$ for the Removal of BPA in Water Samples

Figure 9 shows the HPLC chromatograms of BPA before adsorption (curve a), after adsorption (curve b), and after elution (curve c) for water samples from PP, PET, and PC plastic containers. The application of $MIP_{0.06}@N/C_{3\%}$ for the selective removal and enrichment of BPA from Polypropylene (PP), Polyethylene Terephthalate (PET) and Polycarbonate (PC) plastic containers. The pre-adsorption chromatograms reveal distinct BPA concentrations among the samples, with the PC plastic container exhibiting the most pronounced peak at 6.12 min, followed by the PP container, while the PP container shows the lowest baseline contamination. This BPA distribution correlates directly with the polymer chemistry of each material: polycarbonate is synthesized via condensation of BPA monomers, rendering it inherently prone to hydrolytic degradation and leaching, particularly under high temperatures. In contrast, conventional PP and PET contain BPA primarily as a trace additive rather than a structural component, resulting in substantially lower migration rates. After the post-adsorption by $MIP_{0.06}@N/C_{3\%}$, the BPA peak at 6.12 min demonstrated pronounced decrease across the three samples, confirming the effective removal of BPA by $MIP_{0.06}@N/C_{3\%}$. The imprinted cavities within the $MIP_{0.06}@N/C_{3\%}$ exhibited selective capture for BPA. Notably, the residual peak intensity remains proportional to initial contamination levels, suggesting the adsorption follows a concentration-dependent saturation mechanism. The elution phase chromatograms display sharp, well-resolved BPA peaks, indicating the successful adsorption abilities of $MIP_{0.06}@N/C_{3\%}$ for BPA from diluted samples. The captured analytes can also be efficiently recovered. This enrichment capability is particularly significant for trace-level detection. The consistent elution profile across all samples indicates that $MIP_{0.06}@N/C_{3\%}$ maintains structural integrity and binding capacity regardless of matrix variation, indicating its robustness and applicability for real-world water treatment applications.

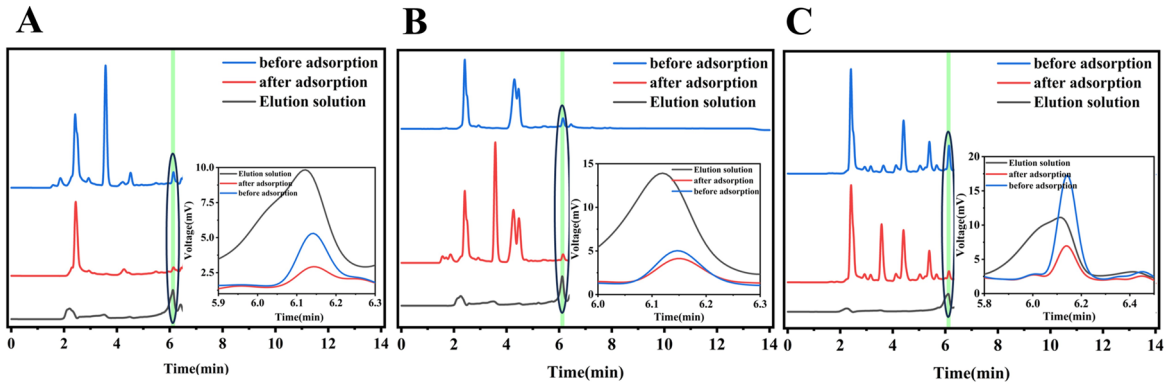

Figure 9. HPLC chromatograms of the pre-adsorption (curve (**A**)), post-adsorption (curve (**B**)) and elution (curve (**C**)) samples from Polypropylene (PP), Polyethylene Terephthalate (PET) and Polycarbonate (PC) plastic containers.

An additional experiment using real industrial wastewater collected from Jiangsu Yangnong Chemical Group Co., Ltd. (Yangzhou, China), which contains BPA as an intrinsic pollutant was studied. Figure 10 shows the UV-vis absorption spectra of the industrial wastewater before and after adsorption. The characteristic absorbance peak of BPA at 278 nm decreased markedly after treatment, while the overall spectral profile of the wastewater remained largely unchanged, confirming the selective removal of BPA. The removal efficiency was calculated to be 92.8%, which is consistent with the high adsorption performance observed under laboratory conditions. These results demonstrate that $MIP_{0.06}$@N/C_3% retains its high adsorption performance even in a complex, non-spiked industrial effluent, highlighting its potential for practical remediation of BPA-contaminated wastewater.

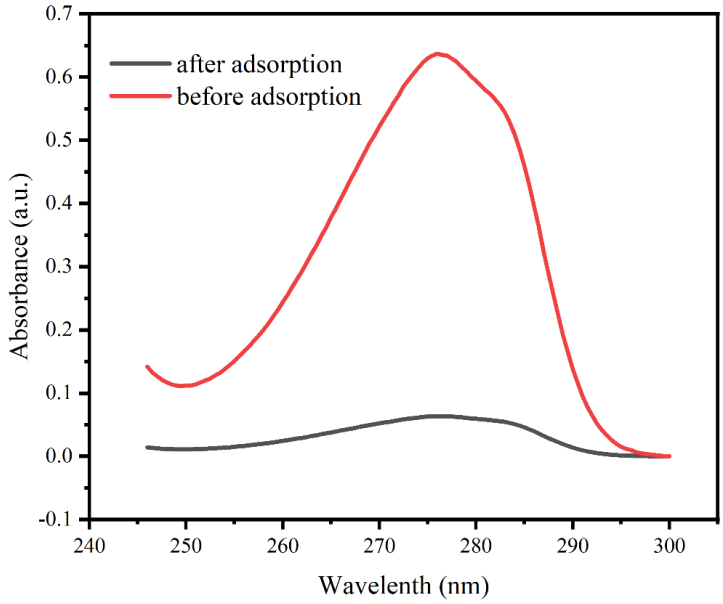

Figure 10. UV-vis spectra of the industrial wastewater containing 9.7 mg/L BPA before and after adsorption with $MIP_{0.06}$@N/C_3% for 8 h.

4. Conclusions

This study developed a hydrogel membrane, MIP@N/C, with good adsorption capacity, selectivity, and reusability for removing biphenyl-structured endocrine-disrupting compounds from water. The hydrophilic MIPs synthesized from AMPS/St ensured strong integration with the hydrogel and improved the mechanical properties and specific adsorption of the hydrogel membrane. The semi-interpenetrating network of the semi-IPN hydrogel constructed from CMCS and NIPAM possessed a tunable pore structure, conducive to enhancing mass transfer rates, thereby promoting the adsorption and desorption of the target pollutant. By blending the aforementioned hydrophilic MIPs into the hydrogel system, an adsorbent membrane material (MIP@N/C) with good mechanical strength and easy separation/recovery was successfully prepared. The membrane exhibited a maximum BPA adsorption capacity of 113.66 mg/g, excellent selectivity over structural analogs, and outstanding reusability

(97.73% capacity retention after 12 cycles). The synergistic combination of specific recognition cavities, porous hydrogel network, and solvent responsive regeneration enables efficient and reversible BPA removal. This design strategy offers a versatile platform for developing next generation adsorptive membranes for water treatment.

Author Contributions

Z.C.: data curation, investigation, methodology, writing—original draft; Y.Z.: data curation, investigation and methodology, writing—original draft; W.X.: formal analysis, investigation and methodology; X.L.: project administration, resources, supervision; L.K.: project administration, resources, supervision; J.Z.: project administration, resources, supervision; S.A.: project administration, resources, supervision; Q.X.: writing—review and editing, project administration, funding acquisition, super vision, visualization, conceptualization. All authors have read and agreed to the published version of the manuscript.

Funding

This research was funded by NSFC (22076161 and 22474123).

Institutional Review Board Statement

Not applicable.

Informed Consent Statement

Not applicable.

Data Availability Statement

The data that support the findings of this study are available from the corresponding authors upon reasonable request.

Conflicts of Interest

The authors declare no conflict of interest.

Use of AI and AI-Assisted Technologies

During the preparation of this work, the authors used DeepSeek to improve the language expression of the work. After using this tool, the authors reviewed and edited the content as needed and take full responsibility for the content of the published article.

References

1. Kang, J.H.; Asai, D.; Toita, R. Bisphenol A (BPA) and Cardiovascular or Cardiometabolic Diseases. *J. Xenobiot.* **2023**, *13*, 775–810. https://doi.org/10.3390/jox13040049.
2. Zhang, H.; Zhang, Y.; Li, J.; et al. Occurrence and Exposure Assessment of Bisphenol Analogues in Source Water and Drinking Water in China. *Sci. Total Environ.* **2019**, *655*, 607–613. https://doi.org/10.1016/j.scitotenv.2018.11.053.
3. Waleed, S.; Haroon, M.; Ullah, N.; et al. A Comprehensive Review on Advanced Trends in Treatment Technologies for Removal of Bisphenol A from Aquatic Media. *Environ. Monit. Assess.* **2025**, *197*, 83. https://doi.org/10.1007/s10661-024-13460-x.
4. Cai, G.P.; Zhang, H.F.; Zhu, R.; et al. Molecularly Imprinted Optical Sensors for Disease Biomarker Analysis: Current Progress and Future Trends. *TrAC Trends Anal. Chem.* **2025**, *194*, 118499. https://doi.org/10.1016/j.trac.2025.118499.
5. Incel, A.; Díez, I.A.; Wierzbicka, C.; et al. Selective Enrichment of Histidine Phosphorylated Peptides Using Molecularly Imprinted Polymers. *Anal. Chem.* **2021**, *93*, 3857–3866. https://doi.org/10.1021/acs.analchem.0c04474.
6. Yu, C.; Ni, J.; Xie, D.; et al. Surface-Confinement Strategy Enabling Ultrahigh Filler Loading in Adsorptive Membranes for Selective TBBPA Separation and Antifouling Performance. *Water Res.* **2026**, *293*, 125408. https://doi.org/10.1016/j.watres.2026.125408.
7. Duan, F.; Chen, C.; Zhao, X.; et al. Water-Compatible Surface Molecularly Imprinted Polymers with Synergy of Bi-Functional Monomers for Enhanced Selective Adsorption of Bisphenol A from Aqueous Solution. *Environ. Sci. Nano* **2016**, *3*, 213–222. https://doi.org/10.1039/c5en00198f.
8. Wang, Z.G.; Luo, X.F.; Song, Z.J.; et al. Microporous Polymer Adsorptive Membranes with High Processing Capacity for Molecular Separation. *Nat. Commun.* **2022**, *13*, 4169. https://doi.org/10.1038/s41467-022-31575-y.

9. Liu, L.; Lan, H.C.; Cui, Y.Q.; et al. A Janus Membrane with Electro-Induced Multi-Affinity Interfaces for High-Efficiency Water Purification. *Sci. Adv.* **2024**, *10*, eadn8696. https://doi.org/10.1126/sciadv.adn8696.
10. Ullah, N.; Ali, Z.; Khan, A.S.; et al. Preparation and Dye Adsorption Properties of Activated Carbon/Clay/Sodium Alginate Composite Hydrogel Membranes. *RSC Adv.* **2024**, *14*, 211–221. https://doi.org/10.1039/d3ra07554k.
11. Zhang, L.Y.; Li, R.Y.; Zheng, S.; et al. Hydrogel-Embedded Vertically Aligned Metal-Organic Framework Nanosheet Membrane for Efficient Water Harvesting. *Nat. Commun.* **2024**, *15*, 9738. https://doi.org/10.1038/s41467-024-54215-z.
12. Dlamini, D.S.; Tesha, J.M.; Vilakati, G.D.; et al. A Critical Review of Selected Membrane- and Powder-Based Adsorbents for Water Treatment: Sustainability and Effectiveness. *J. Clean. Prod.* **2020**, *277*, 123497. https://doi.org/10.1016/j.jclepro.2020.123497.
13. Xiao, Q.Y.; Wang, H.Y.; Wang, L.F.; et al. Interfacial Modification of Hydrogel Composite Membranes for Protein Adsorption with Cavitands as Nano Molecular Containers. *Sep. Purif. Technol.* **2024**, *339*, 126438. https://doi.org/10.1016/j.seppur.2024.126438.
14. Li, J.Y.; Mooney, D.J. Designing Hydrogels for Controlled Drug Delivery. *Nat. Rev. Mater.* **2016**, *1*, 16071. https://doi.org/10.1038/natrevmats.2016.71.
15. Shi, H.R.; Huo, H.X.; Yang, H.X.; et al. Cellulose-Based Dual-Network Conductive Hydrogel with Exceptional Adhesion. *Adv. Funct. Mater.* **2024**, *34*, 2408560. https://doi.org/10.1002/adfm.202408560.
16. Fang, Y.H.; Liang, C.; Liljeström, V.; et al. Toughening Hydrogels with Fibrillar Connected Double Networks. *Adv. Mater.* **2024**, *36*, 2402282. https://doi.org/10.1002/adma.202402282.
17. Wang, Y.Q.; Chen, P.C.; Ding, Y.; et al. Multifunctional Nano-Conductive Hydrogels with High Mechanical Strength, Toughness and Fatigue Resistance as Self-Powered Wearable Sensors and Deep Learning-Assisted Recognition System. *Adv. Funct. Mater.* **2024**, *34*, 2409081. https://doi.org/10.1002/adfm.202409081.
18. Xuan, S.C.; Ding, W.H.; Qiao, F.Z.; et al. Theoretical Simulation-Guided Design and Fabrication of Molecularly Imprinted Hydrogels for Selective Osteopontin Separation. *Food Res. Int.* **2025**, *219*, 117054. https://doi.org/10.1016/j.foodres.2025.117054.
19. Savigni, E.; Girometti, E.; Sisti, L.; et al. Development and Validation of Molecularly Imprinted Polymers with Bio-Based Monomers to Adsorb Carbamazepine from Wastewater. *Molecules* **2025**, *30*, 2533. https://doi.org/10.3390/molecules30122533.
20. Gong, H.; Xu, L.R.; Yang, X.; et al. Construction of a Thermoresponsive Molecularly Imprinted Biomimetic Hydrogel-Based Virus Sensor and Non-Invasive Cyclable Detection of EV71. *Microchim. Acta* **2024**, *191*, 598. https://doi.org/10.1007/s00604-024-06673-x.
21. Hejji, L.; Aoulad El Hadj Ali, Y.; Azzouz, A.; et al. Recent Insights into Molecularly Imprinted Membrane Technology for Removal of Pollutants from Environmental Water: From Organic Molecules to Metal Ions. *J. Water Process Eng.* **2024**, *57*, 104852. https://doi.org/10.1016/j.jwpe.2024.104852.
22. Wu, J.; Li, K.; Zhao, Z. Innovative Nitrogen-Doped Biochar-Derived Ball-Milled Defective In-Situ Amino Biochar Molecularly Imprinted Gels for Selective Removal of BPA: Theoretical Simulation and Mechanistic Insights. *Chem. Eng. J.* **2025**, *505*, 161338. https://doi.org/10.1016/j.cej.2025.161338.
23. Sree Sanker, S.S.; Thomas, S.; Jacob, D.P.; et al. Colorimetric Detection of Bisphenol A in Water: A Smartphone-Based Sensor Using Inverse Opal Molecularly Imprinted Photonic Crystal Hydrogel. *Analyst* **2025**, *150*, 3730–3739. https://doi.org/10.1039/d4an01426j.
24. Wang, X.H.; Deng, L.L.; Long, K.Y.; et al. Molecularly Imprinted Poly(vinylidene fluoride) Electrospinning Membrane for Enhancive Endocrine Disruptor Adsorption and Efficient Dye Removal by Photodegradation. *Environ. Chem. Ecotoxicol.* **2025**, *7*, 882–900. https://doi.org/10.1016/j.enceco.2025.05.002.
25. Jia, R.B.; Zhang, Y.Y.; Li, S.Y.; et al. Magnetic Adsorbents for Removal of Bisphenol A: Design Strategies of Materials and Adsorption Mechanisms. *Chemosphere* **2024**, *368*: 143790. https://doi.org/10.1016/j.chemosphere.2024.143790.
26. Choi, H.Y.; Bae, J.H.; Hasegawa, Y.; et al. Thiol-Functionalized Cellulose Nanofiber Membranes for the Effective Adsorption of Heavy Metal Ions in Water. *Carbohydr. Polym.* **2020**, *234*, 115881. https://doi.org/10.1016/j.carbpol.2020.115881.
27. Wu, Y.L.; Zhao, J.; Wang, C.; et al. A Novel Approach toward Fabrication of Porous Molecularly Imprinted Nanocomposites with Bioinspired Multilevel Internal Domains: Application to Selective Adsorption and Separation Membrane. *Chem. Eng. J.* **2016**, *306*, 492–503. https://doi.org/10.1016/j.cej.2016.07.089.
28. Fan, J.P.; Li, X.; Lai, Z.T.; et al. Electro-Spinning a Calcium Alginate Based Molecular Imprinted Nanofiber Membrane for Selectively Adsorbing Cytochrome c. *Sep. Purif. Technol.* **2025**, *356*, 129877. https://doi.org/10.1016/j.seppur.2024.129877.
29. Zhang, Y.Q.; Tan, X.; Liu, X.; et al. Fabrication of Multilayered Molecularly Imprinted Membrane for Selective Recognition and Separation of Artemisinin. *ACS Sustain. Chem. Eng.* **2019**, *7*, 3127–3137. https://doi.org/10.1021/acssuschemeng.8b04908.
30. Hu, Q.H.; Tang, D.Y.; Wang, X.H.; et al. Molecularly Imprinted MOF/PAN Hybrid Nanofibrous Membranes for Selective Bisphenol A Adsorption and Antibacterial Fouling in Water Treatment. *Sep. Purif. Technol.* **2024**, *328*, 124984. https://doi.org/10.1016/j.seppur.2023.124984.

31. Majcher, M.J.; McInnis, C.L.; Himbert, S.; et al. Photopolymerized Starch-Starch Nanoparticle (SNP) Network Hydrogels. *Carbohydr. Polym.* **2020**, *236*, 115998. https://doi.org/10.1016/j.carbpol.2020.115998.
32. Zewde, B.; Atoyebi, O.; Gugssa, A.; et al. An Investigation of the Interaction between Bovine Serum Albumin-Conjugated Silver Nanoparticles and the Hydrogel in Hydrogel Nanocomposites. *ACS Omega* **2021**, *6*, 11614–11627. https://doi.org/10.1021/acsomega.1c00834.
33. Ullah, R.; Wang, X. Molecular Vibrations of Bisphenol "S" Revealed by FTIR Spectroscopy and Their Correlation with Bisphenol "A" Disclosed by Principal Component Analysis. *Appl. Opt.* **2018**, *57*, D20–D26. https://doi.org/10.1364/AO.57.000D20.
34. Yang, Q.; Gao, D.H.; Miao, R.Y.; et al. Carbon Quantum Dots and Cucurbituril Joining Hands to Achieve Luminescence and Self-Healing Performance in a Hydrogel. *J. Mater. Sci.* **2023**, *58*, 1739–1751. https://doi.org/10.1007/s10853-023-08151-w.
35. Gao, G.; Wang, L.; Cong, Y.; et al. Synergistic pH and Temperature-Driven Actuation of Poly(NIPAM-co-DMAPMA)/Clay Nanocomposite Hydrogel Bilayers. *ACS Omega* **2018**, *3*, 17914–17921. https://doi.org/10.1021/acsomega.8b02979.
36. Sarkaya, K.; Yildirim, M.; Alli, A. One-Step Preparation of Poly(NIPAM-Pyrrole) Electroconductive Composite Hydrogel and Its Dielectric Properties. *J. Appl. Polym. Sci.* **2021**, *138*, e50527. https://doi.org/10.1002/app.50527.
37. Kojima, H. Studies on the Phase Transition of Hydrogels and Aqueous Solutions of Thermosensitive Polymers. *Polym. J.* **2018**, *50*, 411–418. https://doi.org/10.1038/s41428-018-0035-9.
38. Chen, J.H.; Wei, M.B.; Meng, M.J. Advanced Development of Molecularly Imprinted Membranes for Selective Separation. *Molecules* **2023**, *28*, 5764. https://doi.org/10.3390/molecules28155764.
39. Sarfert, F.T.; Etzel, M.R. Mass Transfer Limitations in Protein Separations Using Ion-Exchange Membranes. *J. Chromatogr. A* **1997**, *764*, 3–20. https://doi.org/10.1016/S0021-9673(96)00894-1.
40. Chai, J.Y.; Zheng, J.L.; Yu, H.T.; et al. Recyclable and Selective PVDF-Based Multifunctional Molecular Imprinted Membranes for the Removal of Bisphenol A. *Sep. Purif. Technol.* **2024**, *342*, 127002. https://doi.org/10.1016/j.seppur.2024.127002.
41. Jasni, M.J.F.; Arulkumar, M.; Sathishkumar, P.; et al. Electrospun Nylon 6,6 Membrane as a Reusable Nano-Adsorbent for Bisphenol A Removal: Adsorption Performance and Mechanism. *J. Colloid Interface Sci.* **2017**, *508*, 591–602. https://doi.org/10.1016/j.jcis.2017.08.075.
42. Yao, Y.; Xie, W.Z.; Shen, Y.Z.; et al. Carbon Felt Tailored with Artificial Recognition Elements: An Effective Membrane for Bisphenol A Adsorption and Removal. *J. Mater. Sci.* **2023**, *58*, 18046–18059. https://doi.org/10.1007/s10853-023-09164-1.
43. Liu, M.Y.; Gao, C.P.; Han, R.P.; et al. Assessment of β-Cyclodextrin-Immobilizing Hydrolyzed Polyacrylonitrile Membrane for Enhanced Remediation of Bisphenol A and Tetracyclines: Adsorption and Antibacterial Studies. *J. Clean. Prod.* **2023**, *387*, 135839. https://doi.org/10.1016/j.jclepro.2022.135839.
44. Sun, Z.M.; Yuan, F.; Zhang, X.C.; et al. Design and Synthesis of Organic Rectorite-Based Composite Nanofiber Membrane with Enhanced Adsorption Performance for Bisphenol A. *Environ. Sci. Pollut. Res.* **2019**, *26*, 28860–28870. https://doi.org/10.1007/s11356-019-06069-y.
45. Muhamad, M.S.; Salim, M.R.; Lau, W.J.; et al. Removal of Bisphenol A by Adsorption Mechanism Using PES-SiO_2 Composite Membranes. *Environ. Technol.* **2016**, *37*, 1959–1969. https://doi.org/10.1080/09593330.2015.1137359.
46. Liu, L.F.; Zheng, G.H.; Yang, F.L. Adsorptive Removal and Oxidation of Organic Pollutants from Water Using a Novel Membrane. *Chem. Eng. J.* **2010**, *156*, 553–556. https://doi.org/10.1016/j.cej.2009.04.008.